Acta Biomaterialia 82 (2018) 122–132

Contents lists available at ScienceDirect

Acta Biomaterialia

journal homepage: www.elsevier.com/locate/actabiomat

Full length article

Effects of bisphosphonate ligands and PEGylation on targeted delivery of gold nanoparticles for contrast-enhanced radiographic detection of breast microcalcifications

Lisa E. Cole [a,c], Tracie L. McGinnity [a,c], Lisa E. Irimata [a], Tracy Vargo-Gogola [b,c], Ryan K. Roeder [a,c,*]

[a] Department of Aerospace and Mechanical Engineering, Bioengineering Graduate Program, University of Notre Dame, Notre Dame, IN 46556, USA
[b] Department of Biochemistry and Molecular Biology, Indiana University Simon Cancer Center, Indiana University School of Medicine South Bend, South Bend, IN 46617, USA
[c] Harper Cancer Research Institute, University of Notre Dame, Notre Dame, IN 46556, USA

ARTICLE INFO

Article history:
Received 10 July 2018
Received in revised form 12 September 2018
Accepted 9 October 2018
Available online 11 October 2018

Keywords:
Bisphosphonate
Breast microcalcifications
Computed tomography
Contrast agent
PEGylated gold nanoparticles
Targeted delivery

ABSTRACT

A preclinical murine model of hydroxyapatite (HA) breast microcalcifications (μcals), which are an important clinical biomarker for breast cancer detection, was used to investigate the independent effects of high affinity bisphosphonate (BP) ligands and a polyethylene glycol (PEG) spacer on targeted delivery of gold nanoparticles (Au NPs) for contrast-enhanced radiographic detection. The addition of BP ligands to PEGylated Au NPs (BP-PEG-Au NPs) resulted in five-fold greater binding affinity for targeting HA μcals, as expected, due to the strong binding affinity of BP ligands for calcium. Therefore, BP-PEG-Au NPs were able to target HA μcals *in vivo* after intramammary delivery, which enabled contrast-enhanced radiographic detection of μcals in both normal and radiographically dense mammary tissues similar to previous results for BP-Au NPs, while PEG-Au NPs did not. The addition of a PEG spacer between the BP targeting ligand and Au NP surface enabled improved *in vivo* clearance. PEG-Au NPs and BP-PEG-Au NPs were cleared from all mammary glands (MGs) and control MGs, respectively, within 24–48 h after intramammary delivery, while BP-Au NPs were not. PEGylated Au NPs were slowly cleared from MGs by lymphatic drainage and accumulated in the spleen. Histopathology revealed uptake of PEG-Au NPs and BP-PEG-Au NPs by macrophages in the spleen, liver, and MGs; there was no evidence of toxicity due to the accumulation of NPs in organs and tissues compared with untreated controls for up to 28 days after delivery.

Statement of Significance

Au NP imaging probes and therapeutics are commonly surface functionalized with PEG and/or high affinity targeting ligands for delivery. However, direct comparisons of PEGylated Au NPs with and without a targeting ligand, or ligand-targeted Au NPs with and without a PEG spacer, on *in vivo* targeting efficiency, biodistribution, and clearance are limited. Therefore, the results of this study are important for the rationale design of targeted NP imaging probes and therapeutics, including the translation of BP-PEG-Au NPs which enable improved sensitivity and specificity for the radiographic detection of abnormalities (e.g., μcals) in women with dense breast tissue.

1. Introduction

Breast cancer is the most common cancer and the second leading cause of cancer-related deaths among women in the United States [1]. The five-year survival rate is 98.6% when diagnosed while still confined to the breast, but only 23.3% when diagnosed after metastasizing to distant sites [2]. Therefore, early detection and correct diagnosis of breast cancer is critical for patient survival. Mammographic screening of women ages 40–69 has been associated with a 20–40% reduction in mortality across numerous studies [3,4]. At the same time, mammographic screening can result in false-positives, unnecessary biopsies, and overdiagnosis [3,4].

* Corresponding author at: Department of Aerospace and Mechanical Engineering, Bioengineering Graduate Program, 148 Multidisciplinary Research Building, University of Notre Dame, Notre Dame, IN 46556, USA.
E-mail address: rroeder@nd.edu (R.K. Roeder).

https://doi.org/10.1016/j.actbio.2018.10.014
1742-7061/

Both the sensitivity and specificity of mammography are dramatically decreased with increased breast density [4,5]. Elevated breast density is an independent risk factor for breast cancer and the risk is greatest during the first 12 months following a mammogram, which suggests that this risk results from impaired detection of abnormalities (e.g., microcalcifications) that are masked in mammography by the elevated tissue density [6]. Thus, new imaging methods are needed to improve breast cancer detection in women with elevated radiographic breast density [6].

Ultrasound, magnetic resonance imaging (MRI), and molecular breast imaging (MBI) have been investigated as an adjunct to mammography to improve the detection of abnormalities in women with dense breast tissue [7–9]. However, these methods each have their own limitations in sensitivity, specificity, spatial resolution, radiation dose, availability, cost, and other barriers to widespread adoption [7–9]. Contrast-enhanced dual-energy mammography, which utilizes conventional mammography and iodinated contrast agents to distinguish tumors via vascularity, was recently demonstrated to exhibit detection rates comparable to MRI [10,11]. However, iodinated molecules are limited by potential allergic reactions in patients, rapid clearance, and suboptimal X-ray attenuation, which has motivated investigation of targeted nanoparticle contrast agents for CT [12–16] including optimal compositions for dual-energy mammography [17]. Targeted contrast agents that improve the sensitivity and specificity of existing mammographic instrumentation and screening practices could mitigate the need for adjunct imaging modalities and promote clinical adoption.

Bisphosphonate-functionalized gold nanoparticles (BP-Au NPs) were recently shown to enable improved sensitivity and specificity for contrast-enhanced radiographic detection of breast microcalcifications (μcals) in murine models of normal and radiographically dense mammary tissue [18–20]. μcals are an important early marker for breast cancer and the most common abnormality detected by mammographic screening [21–23]. Targeted delivery of BP-Au NPs to μcals was facilitated by BP ligands, which exhibit high binding affinity for hydroxyapatite (HA) [24], the mineral component of μcals associated with malignant breast lesions [22].

Au NPs are advantageous as an X-ray contrast agent due to exhibiting strong X-ray attenuation, low cytotoxicity *in vivo*, and facile surface functionalization for colloidal stability and molecular targeting [25,26]. Polyethylene glycol (PEG) is commonly used to stabilize Au NPs for improved blood pool stability and circulation upon *in vivo* delivery [25–28]. The importance of high binding affinity ligands for targeted delivery of Au NPs is well-established [25], but the independent effects of a PEG spacer and targeting ligand are not well understood [28]. Direct comparisons of PEGylated Au NPs with and without a targeting ligand, or ligand-targeted Au NPs with and without a PEG spacer, on *in vivo* targeting efficiency, biodistribution, and clearance are lacking. Previous preclinical studies have primarily focused on demonstrating feasibility of targeted delivery to biological targets (e.g., tumors, lymph nodes, brain, etc.) [12–15]. These models are clinically significant but exhibit inherent biological variability in the target that complicates efforts to study the independent effects of a PEG spacer and targeting ligand on the targeting efficiency and clearance.

Therefore, the objective of this study was to investigate the effects of BP ligands on targeted delivery of PEGylated Au NPs in a murine model for contrast-enhanced radiographic detection of breast μcals. The murine μcal model affords relatively precise control and low variability of the engineered μcal targets compared with other *in vivo* models that utilize biologically-derived targets, and was previously used to investigate BP-Au NPs without a PEG spacer [19,20]. Therefore, PEGylated Au NPs with (BP-PEG Au NPs) and without (PEG-Au NPs) a BP targeting ligand, and BP-functionalized Au NPs with (BP-PEG Au NPs) and without (BP-Au NPs) a PEG spacer, were able to be directly compared in a well-characterized and highly-controllable preclinical model. We hypothesized that targeting and contrast-enhanced detection of μcals using BP-PEG-Au NPs would be compromised by the absence of a BP targeting ligand. Previous investigations of contrast-enhanced radiographic detection of breast μcals using BP-Au NPs [18–20] did not utilize a PEG spacer; therefore, we also hypothesized that incorporating a PEG spacer between the Au NP surface and BP targeting ligand would improve biostability and mammary gland clearance compared with BP-Au NPs.

2. Materials and methods

2.1. Synthesis of PEG-Au NPs and BP-PEG-Au NPs

Au NPs were synthesized with a mean NP diameter of ~13 nm and gold concentration of ~0.5 mM in aqueous solution using the citrate reduction method as previously described in detail [29–31]. Au NPs were PEGylated by adding either a monofunctional thiol-PEG (SH-PEG, $CH_3O(CH_2CH_2O)_nCH_2CH_2SH$, 2000 Da, Sigma-Aldrich, St. Louis, MO) or heterobifunctional thiol-PEG-carboxylic acid (SH-PEG-COOH, $CHO_2(CH_2CH_2O)_nCH_2CH_2SH$, 2000 Da, Creative PEGWorks, Winston Salem, NC) to as-synthesized Au NPs at a PEG/Au molar ratio of 0.1 and stirring overnight to allow covalent Au-thiol bonding. BP targeting ligands were added to COOH-PEG-Au NPs by mixing ~20 mg *N*-(3-dimethylaminopropyl)-*N*'-ethylcarbodiimide hydrochloride (EDC, $C_8H_{17}N_3{\cdot}HCl$, 99.0%, Sigma-Aldrich) and ~20 mg *N*-hydroxysulfosuccinimide sodium salt (NHS, $C_4H_4NNaO_6S$, 98%, Sigma-Aldrich) with 30 mL of COOH-PEG-Au NPs at 0.5 mM Au concentration buffered with 0.01 M 2-(*N*-morpholino)ethanesulfonic acid (MES, 99%, $C_6H_{13}NO_4S$, Sigma-Aldrich) under stirring for 25 min. Activated COOH-PEG-Au NPs were collected and separated from unreacted EDC and NHS by centrifugation (Sorvall RD 6 Plus, Thermo Scientific Corporation, Waltham, MA) at 1485*g* for 30 min using molecular weight cutoff filters (Amicon Ultra-15 10 k, Millipore Corporation, Billerica, MA). Activated COOH-PEG-Au NPs were resuspended in phosphate buffered saline (PBS, Amresco, Solon, OH) to 30 mL, 10 mg alendronate sodium trihydrate ($C_4H_{12}NaNO_7P_2{\cdot}3H_2O$, ≥97%, Sigma-Aldrich) was added, and the solution was stirred overnight. All solutions of PEG-Au NPs and BP-PEG-Au NPs were washed thrice by centrifugation at 16,770*g* for 1 h to remove excess PEG and BP prior to further use.

2.2. Characterization

The particle diameter, hydrodynamic diameter, zeta potential, colloidal stability in physiological media, and surface density of PEG and BP were characterized for PEG-Au NPs and BP-PEG-Au NPs. Results were compared to BP-Au NPs and as-prepared, citrate-stabilized Au NPs which were previously prepared and characterized using identical methods [30–32]. The particle diameter distribution was measured from a total of at least 100 randomly selected particles using transmission electron microscopy (TEM, FEI Titan 80-300, Hillsboro, OR) at 80 kV accelerating voltage. TEM specimens were prepared by evaporating drops pipetted from NP solutions onto carbon-coated grids. The hydrodynamic diameter and zeta potential were measured for three replicates of three samples at ambient temperature using dynamic light scattering (DLS, Zetasizer Nano ZS90, Malvern Instruments, Worcestershire, UK) after diluting as-prepared NPs to a final gold concentration of ~0.5 μM in water, which was buffered with 10 mM NaCl (pH 7.2) for zeta potential. Colloidal stability in physiological media was characterized by both DLS and UV–vis spectroscopy (Nanodrop 200C, Thermo Scientific, Wilmington, DE)

after diluting NP solutions with an equal volume of either deionized (DI) water, PBS, or 10% fetal bovine serum (FBS, Omega Scientific, Tarzana, CA) in PBS to a final gold concentration of ~40 mg/L. The hydrodynamic diameter and surface plasmon resonance (SPR) were measured at 0, 2, and 7 days following dilution.

The number of PEG molecules absorbed to Au NP surfaces (PEG/Au NP) was measured for three samples using thermogravimetric analysis (TGA, TGA/DCS-1, Mettler Toledo, Columbus, OH), heating 2–5 mg lyophilized samples of PEG-Au NPs and BP-PEG-Au NPs from 10 to 800 °C at 10 °C/min under nitrogen atmosphere flowing at 50 mL/min. The number of BP molecules per Au NP (BP/Au NP) and NP surface area (BP/nm^2) was calculated from the measured mass ratio of elemental P:Au and particle size distributions, using methods previously described in detail [30]. Assumptions included prolate spheroids for NPs, a P:BP molar ratio of 2:1, and a bulk density of gold of 19.3 g/cm^3. The mass ratio of elemental P:Au was measured for three samples using inductively coupled plasma-optical emission spectroscopy (ICP-OES, Optima 8000, Perkin Elmer, Inc. Waltham, MA) after digesting solutions with 3% v/v aqua regia (3:1 HCl:HNO_3). Calibration curves for ICP-OES were created by diluting certified standard P and Au solutions (Assurance grade, SPEX CertiPrep, Metuchen, NJ).

2.3. Binding affinity to HA

The binding of PEG-Au NPs and BP-PEG-Au NPs to HA crystals was measured in DI water using previously established methods, such that results were compared to previously reported results for BP-Au NPs and Au NPs [30]. Briefly, whisker-shaped HA crystals (10 ± 0.1 mg), exhibiting a mean length and width of ~18 × ~2 μm [33], and varying concentrations of PEG-Au NPs or BP-PEG-Au NPs were added to DI water for a total volume of 15 mL, placed onto a test tube rotator, and allowed to incubate for 4 h. HA crystals with bound Au NPs were separated from unbound Au NPs remaining in solution by centrifugation at ~700*g* for 2 min. The Au concentration in control (no HA crystals) and supernatant solutions was measured by ICP-OES (Optima 8000, PerkinElmer) using the methods described above. All binding tests were performed in triplicate.

Binding isotherms were plotted as the mass of Au NPs bound per mass of HA crystals, V (mg Au/g HA), versus the initial Au concentration, $[S]$ (mg Au/L). Binding isotherms were modeled as a Langmuir isotherm,

$$V = \frac{V_{max}[S]}{K + [S]} \quad (1)$$

where V is the mass of Au NPs bound per mass of HA crystals (mg/g), V_{max} is the maximum surface binding (mg/g), $[S]$ is the initial concentration of gold (mg/L), and K is the equilibrium binding constant (mg/L). K and V_{max} were determined using non-linear least squares regression (JMP 13, SAS Institute, Inc., Cary, NC). V_{max} was also normalized to the specific surface area of HA crystals, V^{*}_{max} (mg Au/m^2 HA), and calculated as the maximum number of Au NPs bound per surface area of HA crystals, $V^{\#}_{max}$ (#/μm^2 HA). The specific surface area of the HA crystals was previously measured to be 5.63 m^2/g [30]; the number of Au NPs was estimated from the bulk density of gold (19.3 g/cm^3) and the measured mean particle size.

Binding of PEG-Au NPs and BP-PEG-Au NPs to HA crystal surfaces was also verified by field emission scanning electron microscopy (FE-SEM, 400 XHR, FEI, Hillsboro, OR) at an accelerating voltage of 5.0 kV and current of 6.3 pA. Samples were prepared by drying collected HA crystals at 50 °C, redispersing in 90% ethanol, pipetting drops onto heated SEM stubs to quickly evaporate the solvent, and coating with 2.5 nm iridium by sputter deposition.

2.4. Murine model of μcals within radiographically dense mammary tissue.

Radiographic detection of μcals was investigated using a previously established transgenic murine model of premalignant breast cancer which recapitulates radiographically dense mammary tissue [20] in combination with previously established methods for creating breast μcals of controlled size within murine mammary glands (MGs) [18–20]. Results were compared to previously reported results for BP-Au NPs using identical models [20]. Female mice positive for the mouse mammary tumor virus-polyoma middle T-antigen (MMTV-PyMT or PyMT) transgene and female wildtype mice negative for the PyMT transgene were obtained by breeding male PyMT mice (Jackson Laboratory, Bar Harbor, ME) on a FVB/NJ background with female FVB mice (Jackson Laboratory) lacking the PyMT transgene. All mice were genotyped for the PyMT transgene using polymerase chain reaction with DNA extracted from ear biopsies at 3 weeks of age. At 7–8 weeks of age, μcals were created within normal and radiographically dense mammary tissue in wildtype and PyMT mice (n = 5/group), respectively, by injecting the left number 4 (4L) MG of anesthetized mice with 50 μL Matrigel (BD Biosciences, San Jose, CA) containing 5.0 mg/mL HA crystals. Matrigel alone was injected into the right number 4 (4R) MG as a negative, contralateral control. All procedures were approved by the Institutional Animal Care and Use Committee at the University of Notre Dame and were conducted in accordance with the guidelines of the U.S. Public Health Service Policy for Humane Care and Use of Laboratory Animals.

2.5. Contrast-enhanced CT

PEG-Au NPs or BP-PEG-Au NPs were administered to anesthetized mice 24 h after creating μcals by intramammary injection of a 100 μL dose containing 50 mM Au NPs, which corresponded to 2 mg Au/mouse, into both the 4L and 4R MG. Mice were imaged *in vivo* under anesthesia by computed tomography (CT, Albira, Bruker Corporation, Billerica, MA) immediately prior to delivering Au NPs (0 h) and longitudinally at 3, 6, 24, and 48 h after delivering Au NPs (n = 5/group/time point). CT images were acquired at 45 kVp and 400 μA for 600 slices with a 250 ms integration time, 125 μm voxel size, and a 0.5 mm aluminum filter. Three-dimensional (3D) CT reconstructions were analyzed using PMOD (v3.17, PMOD Technologies Ltd., Zurich, Switzerland). X-ray attenuation was measured within an animal-specific volume of interest (VOI) determined by contrast between the μcal and surrounding mammary tissue prior to delivery of Au NPs and subsequently mapped onto CT images acquired longitudinally after delivery of Au NPs. The pooled mean (± standard deviation) VOI was 14.3 (0.92) mm^3. Measured grayscale intensities were converted to Hounsfield units (HU) by calibration with air (−1000 HU) and water (0 HU). Two-dimensional (2D) projections of 3D CT reconstructions were created for visualization using VolView (v3.4, Kitware Inc., Clifton Park, NY).

2.6. Biodistribution and histology

Wildtype mice were euthanized at 2, 14, and 28 days after delivery of Au NPs, while PyMT mice were euthanized 2 and 14 days after delivery of Au NPs (n = 5/group/time point). Note that PyMT mice were not permitted to live more than 14 days after delivery of Au NPs (9–10 weeks of age) due to the development of palpable tumors after this time point and the overall tumor burden on mice by 11–12 weeks of age. Selected organs (liver, spleen, kidney, lung, heart, brain, intestine, and skin), tissues (MGs, femora, and peritoneum), and μcals were dissected from three mice in each group, dried overnight in an oven at 37 °C, massed,

and digested in aqua regia (3 HCl:1 HNO_3) for 24 h. The mass of Au in each sample and mass of Ca in μcals was measured using ICP-OES (Optima 8000, Perkin Elmer). Calibration curves were created by diluting certified standard Au and Ca solutions (SPEX CertiPrep). In remaining mice, freshly dissected MGs were immediately fixed in ice cold 4% paraformaldehyde (PFA) for 2 h, while livers and spleens were fixed in neutral buffered formalin for 24 h at room temperature. All tissues were then rinsed with PBS, dehydrated in a graded series of ethanol solutions, embedded in paraffin, sectioned to 4 μm, and stained with hematoxylin and eosin. Stained tissue sections were imaged by transmitted light microscopy (Eclipse ME600, Nikon Instruments, Melville, NY) at 1000X magnification and interpreted by a medical pathologist.

2.7. Statistical methods

All measurements of replicates were reported as the mean (± standard deviation). Differences in the measured NP diameter, hydrodynamic diameter, zeta potential, PEG/Au NP, and BP/Au NP were examined using one-way analysis of variance (JMP 13, SAS Institute Inc., Cary, NC) and *post hoc* comparisons were performed using Tukey's HSD tests. Differences in the hydrodynamic diameter in various physiological media over time were examined using repeated measures ANOVA and *post hoc* comparisons were performed using Tukey's HSD tests. A log-transform of the hydrodynamic diameter was used to provide a normal distribution for analysis. Differences in X-ray attenuation between experimental groups and time points were examined using a mixed model analysis of variance (ANOVA) accounting for longitudinal repeated measures and the nested, random effect of the animal. *Post hoc* comparisons between μcals and negative controls within wildtype and PyMT mice, both before and after delivering PEG-Au NPs or BP-PEG Au NPs, were performed using a paired *t*-test at each longitudinal time point. *Post hoc* comparisons between the X-ray attenuation measured before delivering Au NPs and at longitudinal time points after delivering Au NPs, for both μcals and negative controls within wildtype and PyMT mice, were performed using Tukey's HSD tests. The level of significance for all tests was set at $p < 0.05$.

3. Results and discussion

3.1. Physicochemical characterization

Au NPs were synthesized using the citrate reduction method and surface functionalized with either monofunctional thiol-terminated PEG (PEG-Au NPs, Fig. 1a) or heterobifunctional thiol- and carboxyl-terminated PEG, which was conjugated to alendronate, a BP with a primary amine, using EDC/NHS chemistry (BP-PEG-Au NPs, Fig. 1b). Resulting PEG-Au NPs and BP-PEG-Au NPs were spherical and monodispersed, as characterized by TEM (Fig. 1); the difference in the mean particle diameter was not statistically significant (Table 1). The hydrodynamic diameter distribution measured by DLS was also similar for PEG-Au NPs and BP-PEG-Au NPs (Fig. 1), but the mean hydrodynamic diameter was slightly increased with the addition of BP ligands (Table 1), as expected. The mean hydrodynamic diameter of BP-Au NPs investigated previously was larger still (Table 1), likely due to the presence of weakly associated polyvinyl alcohol molecules which were added as a stabilizer during BP surface functionalization [32]. Importantly, PEG-Au NPs, BP-PEG-Au NPs, and BP-Au NPs exhibited a hydrodynamic diameter that was comparable in magnitude and significantly larger than that for as-prepared, citrate-stabilized Au NPs (Table 1).

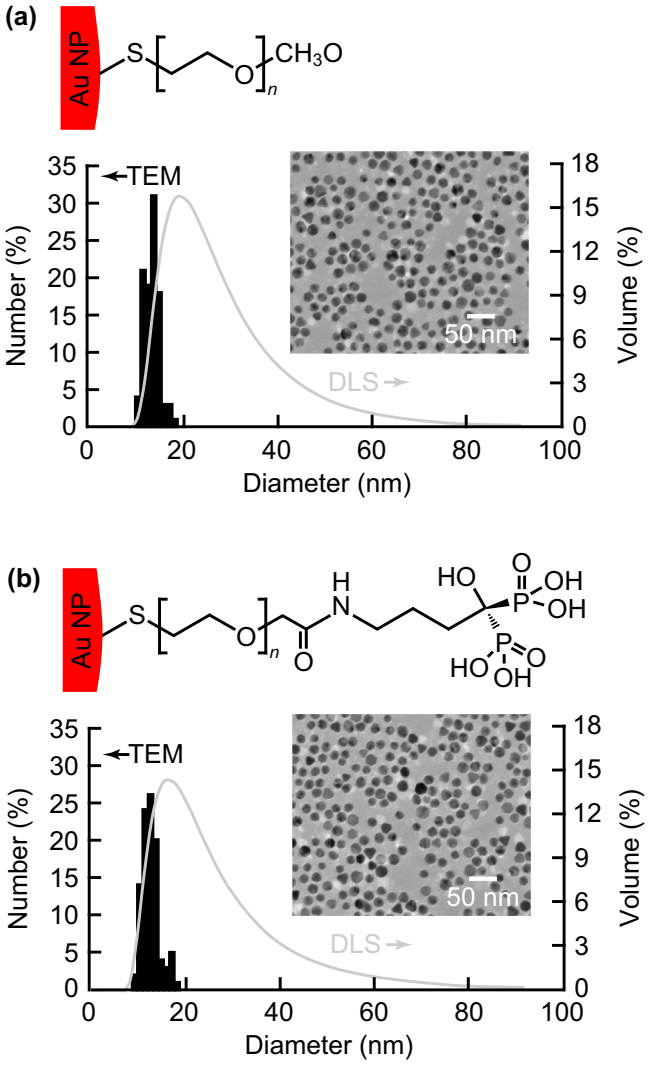

Fig. 1. Au NPs were surface functionalized with either (a) monofunctional thiol-terminated PEG or (b) heterobifunctional thiol-PEG-COOH which was conjugated to alendronate to provide BP ligands for targeting HA μcals. Size distributions measured by TEM (physical diameter) and DLS (hydrodynamic diameter) were similar for both (a) PEG-Au NPs and (b) BP-PEG-Au NPs. Moreover, PEG-Au NPs and BP-PEG-Au NPs were both spherical and monodispersed, as shown in representative TEM micrographs.

The zeta potential measured by DLS was near neutral for PEG-Au NPs and became more negative for BP-PEG-Au NPs due to the charge of BP ligands (Table 1), as expected. The zeta potential of BP-PEG-Au NPs was comparable but more negative than BP-Au NPs, most likely due to a greater density of conjugated BP ligands (Table 1). Surface functionalization decreased the magnitude of the negative zeta potential exhibited by as-prepared, citrate-stabilized Au NPs, due to the displacement and removal of citrate ions (Table 1). Thus, measured changes in both the hydrodynamic diameter and zeta potential indicated successful surface functionalization of the as-prepared Au NPs.

The mean number of PEG molecules adsorbed to Au NP surfaces (PEG/Au NP) was ~900–1000 and was not different between PEG-Au NPs and BP-PEG-Au NPs (Table 1). The measured PEG/Au NP was comparable to previous reported measurements for PEGylated NPs of similar size and PEG molecular weight [27,34,35]. The number of BP molecules per Au NP (BP/Au NP) and NP surface area (BP/nm^2) was ~2500 and 5, respectively, for BP-PEG-Au NPs, which was greater than that for BP-Au NPs (Table 1). This difference was

Table 1
The mean (± standard deviation) NP diameter, hydrodynamic diameter, zeta potential, number of PEG molecules per Au NP (PEG/Au NP), number of BP molecules per Au NP (BP/Au NP), and number of BP molecules per Au NP surface area (BP/nm^2) for PEG-Au NPs, BP-PEG-Au NPs, BP-Au NPs, and Au NPs dispersed in DI water. Groups not connected by the same superscript letter exhibited statistically significant differences ($p < 0.05$, Tukey).

Group	NP Diameter (nm)	Hydrodynamic Diameter (nm)	Zeta Potential (mV)	PEG/Au NP	BP/Au NP	BP/nm^2
PEG-Au NPs	13.1 (1.3)^{ab}	30.9 (2.2)^{a}	−7.2 (2.3)^{a}	965 (240)^{a}	n/a[1]	n/a[1]
BP-PEG-Au NPs	12.6 (1.6)^{a}	33.4 (1.6)^{b}	−17.0 (2.8)^{b}	902 (443)^{a}	2500 (1064)^{a}	4.9 (0.7)^{a}
BP-Au NPs [31,32]	13.2 (0.9)^{b}	43.5 (1.9)^{c}	−11.2 (1.8)^{c}	n/a	1845 (405)^{b}	3.5 (0.3)^{b}
Au NPs [30,32]	13.4 (1.2)^{b}	19.3 (0.3)^{d}	−25.2 (1.9)^{d}	n/a	n/a	n/a

n/a = not applicable; [1]BP/Au NP and BP/nm^2 for PEG-Au NPs were measured to be 43 (14) and 0.08 (0.01), respectively, which reflected the level of background noise in ICP-OES measurements rather than a negligible presence of BP.

most likely due to BP-PEG-Au NPs allowing BP molecules to directly adsorb onto Au NP surfaces, via the primary amine in alendronate, in addition to being conjugated to PEG molecules. In contrast, BP-Au NPs only permitted binding of BP molecules directly onto Au NP surfaces via the primary amine in alendronate [32]. Therefore, PEGylated Au NPs enabled conjugation of a greater number and surface density of BP targeting ligands than was possible by binding BP molecules directly onto Au NP surfaces.

3.2. Colloidal stability in physiologically relevant media

As-prepared PEG-Au NPs and BP-PEG-Au NPs exhibited colloidal stability in physiologically relevant media, including DI water, PBS, and 10% FBS, over a period of 7 days as characterized by DLS and UV–vis spectroscopy. The mean hydrodynamic particle diameter remained unchanged over 7 days in DI water and PBS for both PEG-Au NPs and BP-PEG-Au NPs (Fig. 2). In FBS, the mean hydrodynamic diameter of PEG-Au NPs and BP-PEG-Au NPs was significantly increased by day 7 (Fig. 2a) and day 2 (Fig. 2b), respectively. However, the characteristic SPR peak remained unchanged over 7 days in DI water, PBS, and FBS for both PEG-Au NPs (Fig. 2a) and BP-PEG-Au NPs (Fig. 2b). Therefore, the increase in hydrodynamic diameter measured for BP-PEG-Au NPs in FBS at day 2 (Fig. 2a) was most likely due to non-specific electrostatic adsorption of serum proteins to the negatively-charged BP-PEG-Au NPs (Table 1) and was similar to that previously measured for BP-Au NPs under identical conditions [32]. Moreover, the further increase in hydrodynamic diameter measured for both PEG-Au NPs and BP-PEG-Au NPs in FBS at day 7 was most likely due to coagulation and precipitation of the serum proteins. This explanation was further confirmed by measuring the hydrodynamic diameter of the 10% FBS media in the absence of NPs, which did not exhibit an increase at day 2 but exhibited an increase of similar magnitude by day 7 (data not shown).

3.3. Binding affinity to HA

BP-PEG-Au NPs exhibited significantly greater binding affinity to HA crystals compared with PEG-Au NPs (Fig. 3, Table 2), as expected, due to the high binding affinity of BP ligands chelating calcium ions on HA crystal surfaces [24] compared with a weak, non-specific electrostatic interaction between PEG and HA crystal surfaces. The difference in binding affinity to HA was visually striking in representative SEM micrographs (Fig. 3). The binding isotherm for BP-PEG-Au NPs was accurately modeled by a Langmuir isotherm (Fig. 3) with a correlation coefficient of 0.95 (Table 2). Maximum surface binding constants (V_{max}, V^{*}_{max}, and $V^{\#}_{max}$) were approximately five-fold greater for BP-PEG-Au NPs compared with PEG-Au NPs (Table 2).

The maximum surface binding constants previously measured for BP-Au NPs using identical methods [30] were comparable in magnitude but lower than BP-PEG-Au NPs (Table 2). Therefore, the addition of a PEG spacer between the BP targeting ligand and

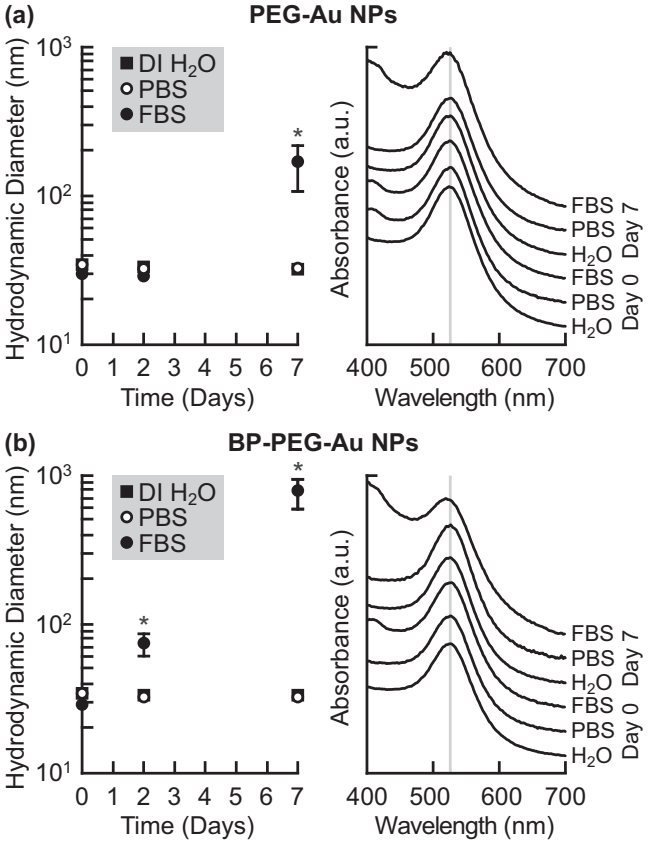

Fig. 2. The colloidal stability of (a) PEG-Au NPs and (b) BP-PEG-Au NPs in physiologically relevant media, including DI water, PBS, and 10% FBS, showing the hydrodynamic diameter measured by DLS at 0, 2, and 7 days and the SPR peak measured by UV–vis spectroscopy at 0 and 7 days. Error bars show one standard deviation of the mean hydrodynamic diameter ($n = 3$ samples/group/time point). Error bars not shown lie within the data point. $^{*}p < 0.05$ vs. all other groups and time points, Tukey. A gray reference line is shown at 527 nm for comparison of SPR peaks in UV–vis spectra.

Au NP surface, and the concomitant increase in BP/Au NP (Table 1), resulted in a greater binding affinity to HA surfaces (Table 2). However, the magnitude of the difference in binding affinity was relatively small compared with the variability in measurements of BP/Au NP and V_{max}. Both BP-PEG-Au NPs and BP-Au NPs possessed an excess of high affinity BP ligands for targeting HA.

3.4. Targeted delivery to μcals within mouse MGs

Contrast-enhanced radiographic detection of μcals targeted by BP-PEG Au NPs was investigated using a previously established and well-characterized model for creating engineered HA μcals within normal (wildtype mice) and radiographically dense (PyMT mice) mammary tissue [18–20]. In all wildtype and PyMT mice,

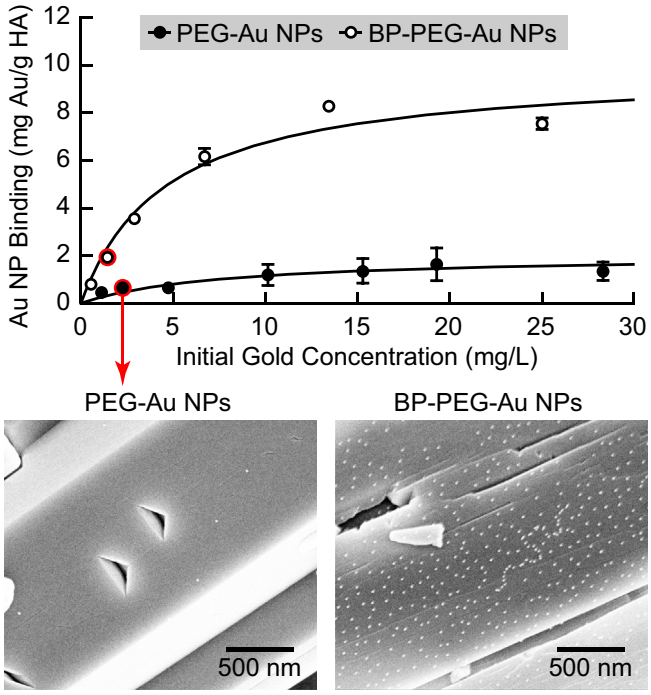

Fig. 3. Binding isotherms and representative SEM micrographs of PEG-Au NPs and BP-PEG-Au NPs adsorbed onto HA crystals in DI water. Error bars show one standard deviation of the mean ($n = 3$ samples/group/time point). Error bars not shown lie within the data point. Experimental data were modeled as a Langmuir isotherm (Eq. (1)) using non-linear least squares regression (lines) and the maximum surface binding constants are reported in Table 2. BP-PEG-Au NPs exhibited significantly greater binding affinity to HA crystals compared with PEG-Au NPs, as expected due to the high binding affinity of BP ligands for calcium ions on HA crystal surfaces.

model μcals were injected into the fat pad of the left number 4 MG while the right number 4 MG served as a negative, contralateral control. Mice were imaged by CT after creating μcals but prior to delivering PEG-Au NPs or BP-PEG-Au NPs (0 h), and longitudinally at 3, 6, 24, and 48 h after delivering PEG-Au NPs or BP-PEG-Au NPs via intramammary injection into both the left and right number 4 MGs.

Prior to delivering PEG-Au NPs or BP-PEG-Au NPs, MGs with μcals exhibited greater X-ray attenuation compared with contralateral controls in wildtype mice (Fig. 4a,b), but not in PyMT mice (Fig. 4c,d) due to the elevated mammary tissue density of PyMT mice masking the detection of μcals [20]. The elevated radiographic density of PyMT mice was previously shown to be due to hyperplastic epithelium and greater amounts of collagen at a pre-malignant stage of development [20,36,37], which recapitulated elevated radiographic density in human breast tissue associated with fibroglandular tissue. Importantly, the addition of engineered μcals within wildtype and PyMT mice was further able to recapitulate the clinical challenges of detecting small abnormalities in dense breast tissue by radiographic imaging. The murine μcal model provided a pathological target with more precise control and lower variability than is possible with biologically-derived targets, which is advantageous for investigating contrast-enhanced detection of a pathological target.

After delivering PEG-Au NPs, MGs with μcals and contralateral controls, in both wildtype and PyMT mice, exhibited a transient increase in X-ray attenuation over 3–6 h and then decreased back to initial levels by 24–48 h (Fig. 4a,c), such that the difference in X-ray attenuation before and 48 h after delivery of PEG-Au NPs was not statistically significant. Moreover, the relative difference in X-ray attenuation (differential contrast, ΔHU) between MGs with μcals and contralateral controls in wildtype mice (Fig. 4a), or the lack of a difference in X-ray attenuation between MGs with μcals and contralateral controls in PyMT mice (Fig. 4c), was generally maintained at all time points after delivery of PEG-Au NPs. These results suggest that PEG-Au NPs were readily cleared from MGs within 24–48 h after intramammary administration and were unable to target HA μcals *in vivo* due to the lack of high binding affinity ligands. Therefore, PEG-Au NPs were unable to enhance the contrast of μcals in either normal or radiographically dense mammary tissues.

After delivering BP-PEG-Au NPs, contralateral control MGs in both wildtype and PyMT mice also exhibited a transient increase in X-ray attenuation over 6 h, and then decreased back to initial levels by 24–48 h (Fig. 4b,d), such that the difference in X-ray attenuation before and 24–48 h after delivery of BP-PEG-Au NPs was not statistically significant. In contrast, MGs with μcals in both wildtype and PyMT mice exhibited an increase in X-ray attenuation that was maintained at each time point after delivering BP-PEG-Au NPs (Fig. 4b,d), such that the difference in X-ray attenuation before and up to 48 h after delivery of BP-PEG-Au NPs was statistically significant. Moreover, MGs with μcals exhibited increased X-ray attenuation compared with contralateral controls at all time points after delivery of BP-PEG-Au NPs. Thus, the relative difference in X-ray attenuation (differential contrast, ΔHU) between MGs with μcals and contralateral controls in both wildtype (Fig. 4b) and PyMT (Fig. 4d) mice was increased at 24–48 h after delivery of BP-PEG-Au NPs compared with before delivery. These results suggest that BP-PEG-Au NPs were readily cleared from control MGs within 24–48 h after intramammary administration and were able to target HA μcals *in vivo* due to high binding affinity BP ligands. Therefore, BP-PEG-Au NPs enabled contrast-enhanced detection of μcals in both normal and radiographically dense mammary tissues. These results also suggest that BP-PEG-Au NPs enabled improved specificity for detecting μcals in normal mammary tissues (Fig. 4b) and improved sensitivity for detecting μcals that were otherwise undetectable in radiographically dense mammary tissues (Fig. 4d).

The ability of BP-PEG-Au NPs to target HA μcals and enhance radiographic contrast was not unlike previous results for BP-Au NPs using the same *in vivo* model [20]. However, BP-PEG-Au NPs were more readily cleared from control MGs compared with BP-Au NPs. The delivery of BP-Au NPs to control MGs resulted in an increase in X-ray attenuation that was maintained at each subsequent time point, such that the difference in X-ray

Table 2
Binding constants for PEG-Au NPs, BP-PEG-Au NPs, BP-Au NPs, and Au NPs adsorbed onto HA crystals in DI water determined by non-linear least squares regression of Langmuir adsorption isotherms, where V_{max} is the maximum surface binding (mg Au/g HA), V^{*}_{max} is the maximum surface binding normalized to the specific surface area of HA crystals (mg Au/m^2 HA), $V^{\#}_{max}$ is the maximum number of Au NPs bound per surface area of HA crystals (#/μm^2 HA), and R^2 is the correlation coefficient for the regression. The 95% confidence interval for V_{max} is shown in square brackets.

Group	V_{max} (mg/g)	V^{*}_{max} (mg/m^2)	$V^{\#}_{max}$ (#/μm^2)	R^2
PEG-Au NPs	2.1 [1.2, 2.9]	0.4	17	0.62
BP-PEG-Au NPs	9.8 [8.8, 10.9]	1.7	86	0.96
BP-Au NPs [30]	7.7 [6.9, 8.6]	1.4	65	0.95
Au NPs [30]	0.4 [0.2, 0.5]	0.1	3	0.75

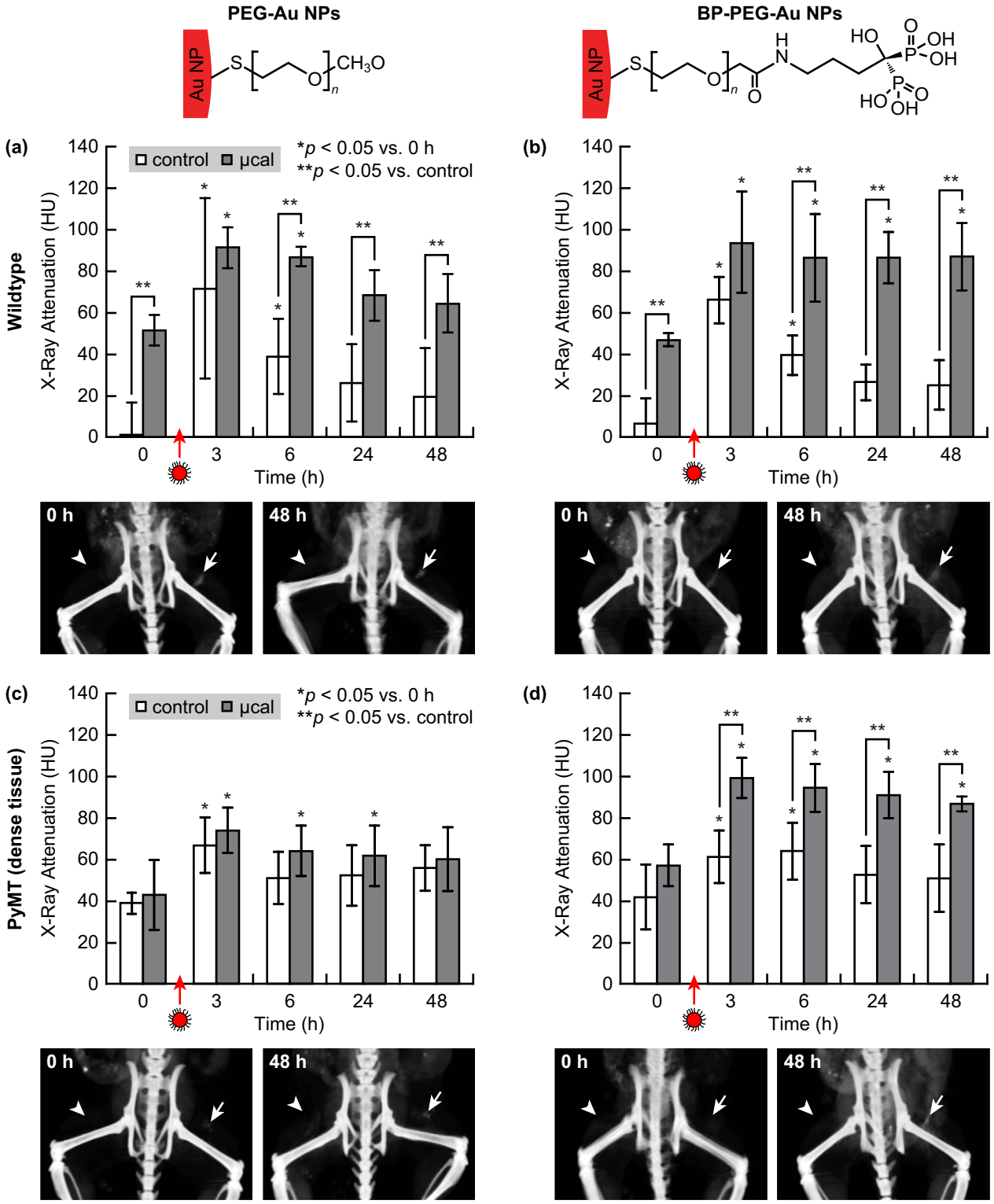

Fig. 4. The X-ray attenuation (HU) measured *in vivo* from 3D CT reconstructions for HA μcals compared with negative, contralateral controls in (a,b) wildtype and (c,d) PyMT mice exhibiting radiographically dense mammary tissue before (0 h) and longitudinally at 3, 6, 24, and 48 h after intramammary delivery of (a,c) PEG-Au NPs and (b,d) BP-PEG-Au NPs. Error bars show one standard deviation of the mean ($n = 5$ mice/group). $^{*}p < 0.05$ vs. 0 h, Tukey. $^{**}p < 0.05$ μcal vs. control, paired *t*-test. Note that a differential contrast (ΔHU) of at least 30 HU has been suggested to be necessary for visibly apparent enhanced-contrast in CT [38,39]. Representative 2D grayscale CT image projections show HA μcals within 4L MGs (arrows) compared with negative, contralateral controls in 4R MGs (arrowheads), before (0 h) and 48 h after delivering PEG-Au NPs and BP-PEG-Au NPs. BP-PEG-Au NPs enabled contrast-enhanced detection of μcals in both normal (wildtype) and radiographically dense (PyMT) mammary tissues, while PEG-Au NPs did not. PEG-Au NPs and BP-PEG-Au NPs were cleared from all MGs and control MGs, respectively, within 24–48 h after delivery.

attenuation before and up to 48 h after delivery of BP-Au NPs was statistically significant [20]. In contrast, the delivery of BP-PEG-Au NPs to control MGs resulted in a transient increase in X-ray attenuation that returned to initial levels by 24–48 h (Fig. 4b,d), such that the difference in X-ray attenuation before and 24–48 h after delivery of BP-PEG-Au NPs was not statistically significant. This

result suggests that the addition of a PEG spacer between the BP targeting ligand and Au NP surface enabled improved clearance *in vivo*.

3.5. Biodistribution and histology

The biodistribution of PEG-Au NPs and BP-PEG-Au NPs in various organs and tissues was measured at 2, 14, and 28 days after delivery in wildtype mice, and at 2 days after delivery in PyMT mice (Fig. 5). The 14 and 28 day time points were not completed for PyMT mice due to the development of nonpalpable tumors by 14 days after delivery of Au NPs (9–10 weeks of age) and the overall tumor burden on mice by 11–12 weeks of age. The highest concentrations of Au were measured in μcals, MGs, the surrounding skin, and peritoneum at every time point for both PEG-Au NPs and BP-PEG-Au NPs in both WT and PyMT mice (Fig. 5). The relatively high concentration of Au at these sites was expected due to the localized, intramammary administration of Au NPs. The concentration of Au in μcals was greater for BP-PEG-Au NPs (Fig. 5b) compared with PEG-Au NPs (Fig. 5a), and was maintained over 28 days, confirming targeting of HA μcals by BP-PEG-Au NPs. Thus, important trends observed in X-ray attenuation measurements at the 48 h time point (Fig. 4) were in good agreement with the measured Au biodistribution at the same time point (Fig. 5). This suggests that CT can be used to non-invasively measure the *in vivo* biodistribution of NPs, especially with the advent of photon-counting spectral CT enabling *k*-edge imaging [40].

The concentration of Au in MGs and the surrounding skin and peritoneum exhibited little change over 28 days (Fig. 5). Interestingly, the concentration of Au increased over time in the spleen (Fig. 5), while concentrations of Au measured in the liver, kidneys, lungs, heart, brain, intestines, and femora were low, often within the measurement noise. These results suggest that after intramammary administration, Au NPs were slowly cleared from MGs by lymphatic drainage and accumulated in the spleen. In contrast, there was relatively little or no clearance from MGs to the liver and kidneys, as is commonly observed after intravenous delivery [25,27,41–43]. Thus, the route of administration had a profound effect on the *in vivo* biodistribution of PEGylated Au NPs.

The biodistribution previously measured for BP-Au NPs using the same *in vivo* model and characterization methods revealed comparable concentrations of Au in the MGs and the surrounding skin and peritoneum, but much lower accumulation in the spleen [20]. Thus, PEG-Au NPs and BP-PEG-Au NPs were more readily cleared from MGs and surrounding tissues to the spleen compared with BP-Au NPs. This result suggests that the addition of a PEG spacer between the BP targeting ligand and Au NP surface enabled improved clearance from MGs *in vivo*.

Lymphatic clearance of NPs has been previously reported after subcutaneous delivery [44–47], which could be expected to exhibit a similar clearance route as intramammary delivery. Inguinal lymph nodes in the number 4 MGs were visually observed to be dark red in color upon dissection of the MGs. This observation suggests that after intramammary delivery PEGylated Au NPs were

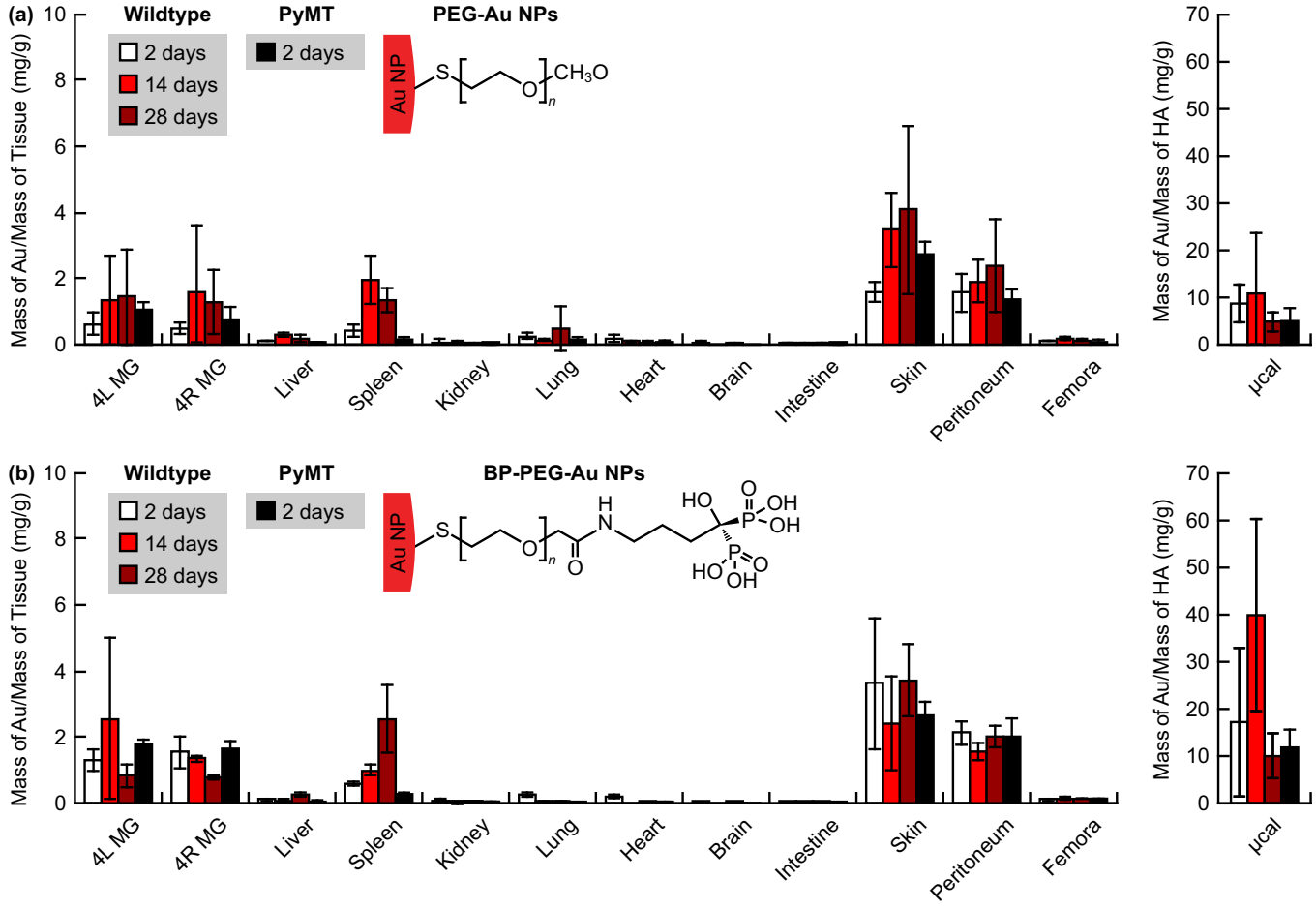

Fig. 5. The biodistribution of Au measured within organs, tissues, and μcals in wildtype mice at 2, 14, and 28 days after intramammary delivery of (a) PEG-Au NPs and (b) BP-PEG-Au NPs, and in PyMT mice exhibiting radiographically dense mammary tissue at 2 days after intramammary delivery of (a) PEG-Au NPs and (b) BP-PEG-Au NPs. Error bars show one standard deviation of the mean (n = 3/group/time point). PEG-Au NPs and BP-PEG-Au NPs cleared from MGs to the surrounding skin and peritoneum, and accumulated in the spleen more than the liver and kidneys.

transported to the resident lymph nodes [48]. However, the concentration of Au in the lymph nodes over time was not measured separately from the entire MG due to the small mass of tissue. Transport of PEGylated Au NPs from resident lymph nodes to the spleen occurred via slow drainage from lymphatic vessels into the blood pool which is filtered by the spleen [49]. PEGylated Au NPs accumulated in the spleen (Fig. 5), where they were taken up by splenic macrophages (Fig. 6) [49,50]. The mechanism for accumulation of PEGylated Au NPs in the spleen after intramammary delivery vs. the liver and kidneys after intravenous

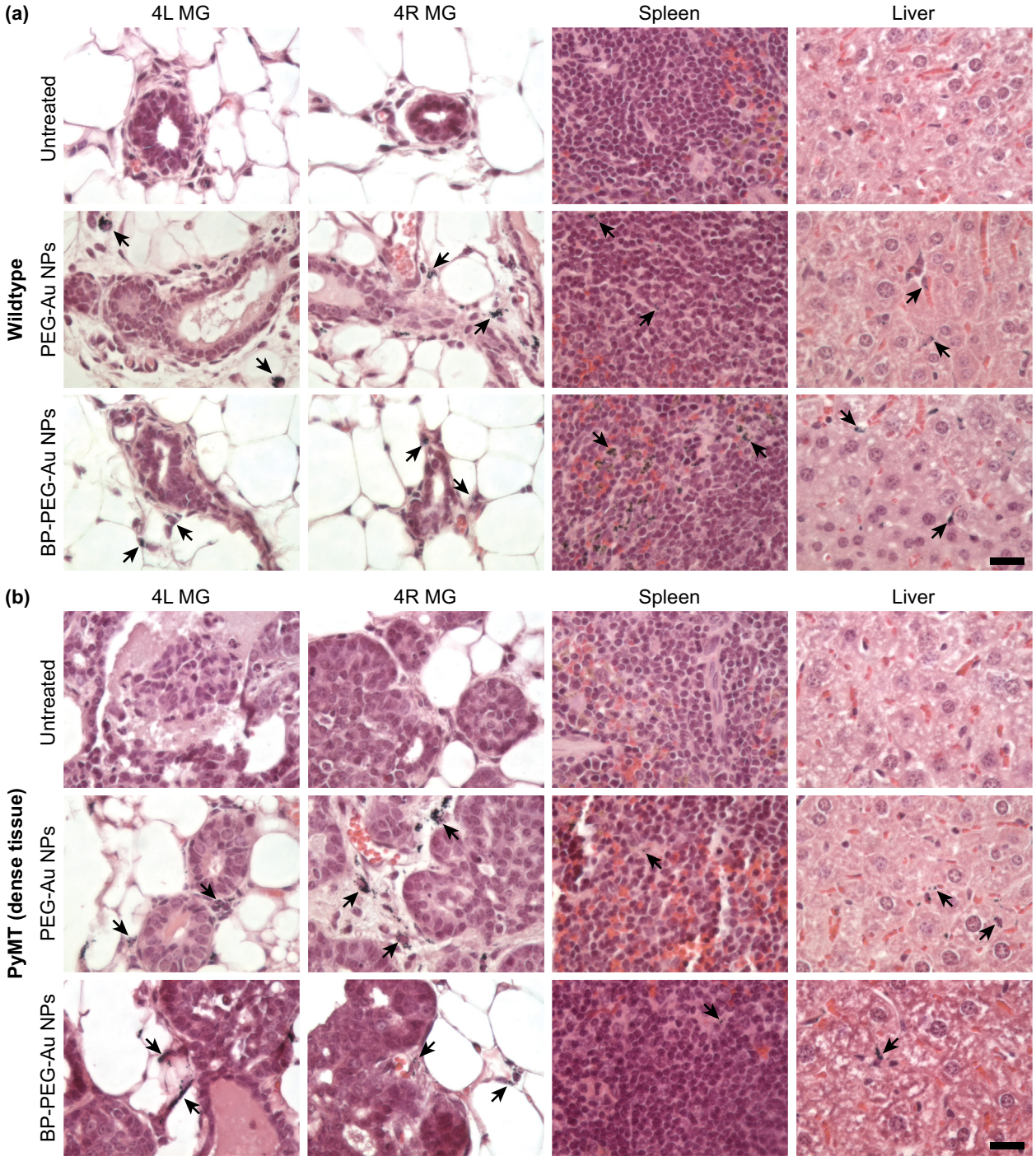

Fig. 6. Representative transmitted light optical micrographs of histological sections prepared from the MGs, spleen and liver of (a) wildtype mice and (b) PyMT mice exhibiting radiographically dense mammary tissue before (untreated) and 14 days after intramammary delivery of PEG-Au NPs and BP-PEG-Au NPs. Representative micrographs at 2 and 28 days are available in Fig. 6S as supplementary content. Arrows highlight PEG-Au NPs and BP-PEG-Au NPs (black in color) taken up by macrophages. No changes were apparent in the cell or tissue morphology between treated (PEG-Au NPs and BP-PEG-Au NPs) and untreated tissues for up to 28 days after delivery, which suggests there was no cytoxicity. Normal ductal structures are shown in wildtype mice, while PyMT mice exhibited hyperplastic epithelium surrounding ductal structures.

delivery is not entirely clear. One possible explanation is that PEGylated Au NPs are opsonized by antibodies in the lymph fluid which are recognized by the spleen, but the role of the spleen in the pharmacokinetics of NPs is not yet well-understood [49].

The total amount of Au (mg) measured in all the organs and tissues did not change with time (data not shown). This suggests that PEG-Au NPs and BP-PEG-Au NPs were not cleared from mice during the time period studied, but instead redistributed throughout the body. Moreover, renal clearance was not expected since the size of the Au NPs in this study was larger than the glomerular filtration system cutoff [51].

The histopathology of various organs and tissues was examined at 2, 14, and 28 days after delivering PEG-Au NPs and BP-PEG-Au NPs in wildtype mice, and at 2 and 14 days after delivering PEG-Au NPs and BP-PEG-Au NPs in PyMT mice (Fig. 6). There were no apparent changes in tissue or cellular morphology, and thus no evidence of tissue level toxicity, in the MGs, spleen, and liver due to the accumulation of PEG-Au NPs or BP-PEG-Au NPs at any time point compared with untreated controls. PEG-Au NPs and BP-PEG-Au NPs were taken up by macrophages in the MGs, spleen, and liver (arrows, Fig. 6), and this accumulation appeared to increase with time. Intracellular PEG-Au NPs and BP-PEG-Au NPs appeared to be highly concentrated within the cytoplasm but did not appear to enter the nucleus. There has been a paucity of data for the long term (weeks) *in vivo* cytotoxicity of Au NPs at concentrations necessary for use as an X-ray contrast agent, particularly for the liver and spleen, which typically accumulate the highest concentrations of Au NPs after delivery [25]. Therefore, the results of this study aid in filling a gap in the literature and are promising for clinical translation of PEG-Au NPs and BP-PEG-Au NPs given that the MGs and spleen were exposed to a relatively high concentration of Au NPs over 28 days (Fig. 5).

The absence of any histological evidence of tissue level toxicity over 28 days exposure to relatively high concentrations of Au NPs is promising but warrants further analysis. For example, the spleen was exposed to a mass concentration of Au that was approximately ~6000X greater than that previously shown to result in no cellular or genetic toxicity [50,52]. Additionally, the mass concentration of Au in the liver was much lower than the MGs and spleen but was still ~2X greater than that previously reported to cause acute liver toxicity and genetic changes indicative of an immune response [50,52,53]. Therefore, the results of this study must be followed with more detailed cellular and molecular level analyses. Nonetheless, the results of this study are significant due to providing a relatively long-term evaluation of the *in vivo* biodistribution and cytoxocity of Au NPs at a dose suitable for use an X-ray contrast agent, which is significantly greater than doses typically used to study the *in vitro* and *in vivo* toxicity of Au NPs [25].

4. Conclusions

The addition of BP ligands to PEGylated Au NPs (BP-PEG-Au NPs) resulted in five-fold greater binding affinity for targeting HA μcals, as expected, due to the strong binding affinity of BP ligands for calcium. Therefore, BP-PEG-Au NPs were able to target HA μcals *in vivo* after intramammary delivery, which enabled contrast-enhanced radiographic detection of μcals in both normal and radiographically dense mammary tissues similar to previous results for BP-Au NPs, while PEG-Au NPs did not. The addition of a PEG spacer between the BP targeting ligand and Au NP surface enabled improved *in vivo* clearance. PEG-Au NPs and BP-PEG-Au NPs were cleared from all MGs and control MGs, respectively, within 24–48 h after intramammary delivery, while BP-Au NPs were not. PEGylated Au NPs were slowly cleared from MGs by lymphatic drainage and accumulated in the spleen. Histopathology revealed uptake of PEG-Au NPs and BP-PEG-Au NPs by macrophages in the spleen, liver, and MGs; there was no evidence of toxicity due to the accumulation of NPs in organs and tissues compared with untreated controls for up to 28 days after delivery.

Acknowledgments

This work was supported by the Walther Cancer Foundation through a Seeding Research in Cancer (SRC) Grant and an Engineering Novel Solutions to Cancer's Challenges at the Interdisciplinary Interface (ENSCCII) Training Grant. This work was also supported by the National Science Foundation (DMR-1309587), Kelly Cares Foundation, and St. Joseph Health System. The authors acknowledge the Freimann Life Science Center at the University of Notre Dame for the care of animals; the Notre Dame Integrated Imaging Facility for the use of CT, electron microscopy, and Histology Core; and the Center for Environmental Science and Technology at the University of Notre Dame for use of the ICP-OES. Finally, Dr. William Kaliney, M.D., is acknowledged for sharing his expertise in pathology and interpreting the histological sections.

Data availability

The raw and processed data required to reproduce these findings are available to download from https://doi.org/10.17632/pd7wrgwdjz.1.

Appendix A. Supplementary data

Supplementary data to this article can be found online at https://doi.org/10.1016/j.actbio.2018.10.014.

References

[1] R.D. Siegel, K.D. Miller, A. Jemal, Cancer statistics, CA Cancer J. Clin. 67 (2017) (2017) 7–30.
[2] R.A. Smith, S.W. Duffy, L. Tabar, Breast cancer screening: the evolving evidence, Oncology 26 (2012) 471–486.
[3] K.C. Oeffinger, E.T.H. Fontham, R. Etzioni, A. Herzig, J.S. Michaelson, Y.T. Shih, L. C. Walter, T.R. Church, C.R. Flowers, S.J. LaMonte, A.M.D. Wolf, C. DeSantis, J. Lortet-Tieulent, K. Andrews, D. Manassaram-Baptiste, D. Saslow, R.A. Smith, O. W. Brawley, R. Wender, Breast cancer screening for women at average risk. 2015 guideline update from the American Cancer Society, JAMA 314 (2015) (2015) 1599–1614.
[4] A.L. Siu, Screening for breast cancer: US preventive services task force recommendation statement, Ann. Intern. Med. 164 (2016) 279–296.
[5] P.A. Carney, D.L. Miglioretti, B.C. Yankaskas, K. Kerlikowske, R. Rosenberg, C.M. Rutter, B.M. Geller, L.A. Abraham, S.H. Taplin, M. Dignan, G. Cutter, Individual and combined effects of age, breast density, and hormone replacement therapy use on the accuracy of screening mammography, Ann. Intern. Med. 138 (2003) 168–175.
[6] N.F. Boyd, H. Guo, L.J. Martin, L. Sun, J. Stone, E. Fishell, R.A. Jong, G. Hislop, A. Chiarelli, S. Minkin, M.J. Yaffe, Mammographic density and the risk and detection of breast cancer, N. Engl. J. Med. 356 (2007) 227–236.
[7] C.H. Lee, D.D. Dershaw, D. Kopans, P. Evans, B. Monsees, D. Monticciolo, R.J. Brenner, L. Bassett, W. Berg, S. Feig, E. Hendrick, Breast cancer screening with imaging: recommendations from the Society of Breast Imaging and the ACR on the use of mammography, breast MRI, breast ultrasound, and other technologies for the detection of clinically occult breast cancer, J. Am. Coll. Radiol. 7 (2010) 18–27.
[8] D.J. Rhodes, C.B. Hruska, A.L. Conners, C.L. Tortorelli, R.W. Maxwell, K.N. Jones, A.Y. Toledano, M.K. O'Connor, Molecular breast imaging at reduced radiation dose for supplemental screening in mammographically dense breasts, Am. J. Roentgenol. 204 (2015) 241–251.
[9] J.S. Drukteinis, B.P. Mooney, C.I. Flowers, R.A. Gatenby, Beyond mammography: new frontiers in breast cancer screening, Am. J. Med. 126 (2013) 472–479.
[10] U. Lalji, M. Lobbes, Contrast-enhanced dual-energy mammography: a promising new imaging tool in breast cancer detection, Women's Health (Lond.) 10 (2014) 289–298.
[11] M.F. Covington, V.J. Pizzitola, R. Lorans, B.A. Pockaj, D.W. Northfelt, C.M. Appleton, B.K. Patel, The future of contrast-enhanced mammography, Am. J. Roentgenol. 210 (2018) 292–300.
[12] W. Eck, A.I. Nicholson, H. Zentgraf, W. Semmler, S. Bartling, Anti-CD4-targeted gold nanoparticles induce specific contrast enhancement of peripheral lymph nodes in X-ray computed tomography of live mice, Nano Lett. 10 (2010) 2318–2322.

[13] T. Reuveni, M. Motiei, Z. Romman, A. Popovtzer, R. Popovtzer, Targeted gold nanoparticles enable molecular CT imaging of cancer: an in vivo study, Int. J. Nanomed. 6 (2011) 2859–2864.
[14] C. Peng, J. Qin, B. Zhou, Q. Chen, M. Shen, M. Zhu, X. Lu, X. Shi, Targeted tumor CT imaging using folic acid-modified PEGylated dendrimer-entrapped gold nanoparticles, Polym. Chem. 4 (2013) 4412–4424.
[15] M. Shilo, M. Motiei, P. Hana, R. Popovtzer, Transport of nanoparticles through the blood–brain barrier for imaging and therapeutic applications, Nanoscale 6 (2014) 2146–2152.
[16] H.K. Gaikwad, D. Tsvirkun, Y. Ben-Nun, E. Merquiol, R. Popovtzer, G. Blum, Molecular imaging of cancer using X-ray computed tomography with protease targeted iodinated activity-based probes, Nano Lett. 18 (2018) 1582–1591.
[17] P.C. Naha, C.K. Lau, J.C. Hsu, M. Hajfathalian, S. Mian, P. Chhour, L. Uppulari, E.S. MacDonald, A.D.A. Maidment, D.P. Cormode, Gold silver alloy nanoparticles (GSAN): An imaging probe for breast cancer screening with dual-energy mammography or computed tomography, Nanoscale 8 (2016) 13740–13754.
[18] L.E. Cole, T. Vargo-Gogola, R.K. Roeder, Bisphosphonate-functionalized gold nanoparticles for contrast-enhanced X-ray detection of breast microcalcifications, Biomaterials 35 (2014) 2312–2321.
[19] L.E. Cole, T. Vargo-Gogola, R.K. Roeder, Contrast-enhanced X-ray detection of breast microcalcifications in a murine model using targeted gold nanoparticles, ACS Nano 8 (2014) 7486–7496.
[20] L.E. Cole, T. Vargo-Gogola, R.K. Roeder, Contrast-enhanced X-ray detection of microcalcifications in radiographically dense mammary tissue using targeted gold nanoparticles, ACS Nano 9 (2015) 8923–8932.
[21] A. Venkatesan, P. Chu, K. Kerlikowske, E.A. Sickles, R. Smith-Bindman, Positive predictive value of specific mammographic findings according to reader and patient variables, Radiology 250 (2009) 648–657.
[22] M.P. Morgan, M.M. Cooke, G.M. McCarthy, Microcalcifications associated with breast cancer: An epiphenomenon or biologically significant feature of selected tumors?, J Mammary Gland Biol. Neoplasia 10 (2005) 181–187.
[23] H.D. Cheng, X. Cai, X. Chen, L. Hu, X. Lou, Computer-aided detection and classification of microcalcifications in mammograms: a survey, Pattern Recogn. 36 (2003) 2967–2991.
[24] L.E. Cole, T. Vargo-Gogola, R.K. Roeder, Targeted delivery to bone and mineral deposits using bisphosphonate ligands, Adv. Drug Delivery Rev. 99 (2016) 12–27.
[25] L.E. Cole, R.D. Ross, J.M.R. Tilley, T. Vargo-Gogola, R.K. Roeder, Gold nanoparticles as contrast agents in X-ray imaging and computed tomography, Nanomedicine 10 (2015) 321–341.
[26] H. Lusic, M.W. Grinstaff, X-ray computed tomography contrast agents, Chem. Rev. 131 (2013) 1641–1666.
[27] J.V. Jokerst, T. Lobovkina, R.N. Zare, S.S. Gambhir, Nanoparticle PEGylation for imaging and therapy, Nanomedicine 6 (2011) 715–728.
[28] K.F. Pirollo, E.H. Chang, Does a targeting ligand influence nanoparticle tumor localization or uptake?, Trends Biotechnol 26 (2008) 552–558.
[29] Z. Zhang, R.D. Ross, R.K. Roeder, Preparation of functionalized gold nanoparticles as a targeted X-ray contrast agent for damaged bone tissue, Nanoscale 2 (2010) 582–586.
[30] R.D. Ross, R.K. Roeder, Binding affinity of surface functionalized gold nanoparticles to hydroxyapatite, J. Biomed. Mater. Res. 99A (2011) 58–66.
[31] R.D. Ross, L.E. Cole, J.M.R. Tilley, R.K. Roeder, Effect of functionalized gold nanoparticle size on X-ray attenuation and binding affinity to hydroxyapatite, Chem. Mater. 26 (2014) 1187–1194.
[32] R.D. Ross, L.E. Cole, R.K. Roeder, Relative binding affinity of carboxylate-, phosphonate-, and bisphosphonate-functionalized gold nanoparticles targeted to damages bone tissue, J. Nanopart. Res. 14 (2012) 1175.
[33] R.K. Roeder, G.L. Converse, H. Leng, W. Yue, Kinetic effects on hydroxyapatite whiskers synthesized by the chelate decomposition method, J. Am. Ceram. Soc. 89 (2006) 2096–2104.
[34] J. Manson, D. Kumar, B.J. Meenan, D. Dixon, Polyethylene glycol functionalized gold nanoparticles: the influence of capping density on stability in various media, Gold Bull. 44 (2011) 99–105.
[35] K. Rahme, L. Chen, R.G. Hobbs, M.A. Morris, C. O'Driscoll, J.D. Holmes, PEGylated gold nanoparticles: polymer quantification as a function of PEG lengths and nanoparticle dimensions, RSC Adv. 3 (2013) 6085–6094.
[36] E.Y. Lin, J.G. Jones, P. Li, L. Zhu, K.D. Whitney, W.J. Muller, J.W. Pollard, Progression to malignancy in the polyoma middle T oncoprotein mouse breast cancer model provides a reliable model for human diseases, Am. J. Pathol. 163 (2003) 2113–2126.
[37] M. Hariri, G.A. Wood, M.A. DiGrappa, M. MacPherson, S.A. Backman, M.J. Yaffe, T.W. Mak, N.F. Boyd, R. Khokha, Experimental manipulation of radiographic density in mouse mammary gland, Breast Cancer Res. 6 (2004) R540–R545.
[38] W. Krause, Delivery of diagnostic agents in computed tomography, Adv. Drug Delivery Rev. 37 (1999) 159–173.
[39] M.W. Galper, M.T. Saung, V. Fuster, E. Roessl, A. Thran, R. Proksa, Z.A. Fayad, D. P. Cormode, Effect of computed tomography scanning parameters on gold nanoparticle and iodine contrast, Invest. Radiol. 47 (2012) 475–481.
[40] S. Si-Mohamed, D.P. Cormode, D. Bar-Ness, M. Sigovan, P.C. Naha, J.-B. Langlois, L. Chalabreysse, P. Coulon, I. Blevis, E. Roessl, K. Erhard, L. Boussel, P. Douek, Evaluation of spectral photon counting computed tomography K-edge imaging for determination of gold nanoparticle biodistribution *in vivo*, Nanoscale 9 (2017) 18246–18257.
[41] G. Sonavane, K. Tomoda, K. Makino, Biodistribution of colloidal gold nanoparticles after intravenous administration: effect of particle size, Colloids Surf. B: Biointerfaces 66 (2008) 274–280.
[42] S.K. Balasubramanian, J. Jittiwat, J. Manikandan, C.-N. Ong, L.E. Yu, W.-Y. Ong, Biodistribution of gold nanoparticles and gene expression changes in the liver and spleen after intravenous administration in rats, Biomaterials 31 (2010) 2034–2042.
[43] S. Hirn, M. Semmler-Behnke, C. Schleh, A. Wenk, J. Lipka, M. Schäffler, S. Takenaka, W. Möller, G. Schmid, U. Simon, W.G. Kreyling, Particle size-dependent and surface charge-dependent biodistribution of gold nanoparticles after intravenous administration, Eur. J. Pharm. Biopharm. 77 (2011) 407–416.
[44] S.M. Moghimi, A.R. Rajabi-Siahboomi, Advanced colloid based systems for efficient delivery of drugs and diagnostic agents to the lymphatic tissues, Prog. Biophys. Mol. Biol. 65 (1996) 221–249.
[45] O. Rabin, J. Manuel Perez, J. Grimm, G. Wojtkiewicz, R. Weissleder, An X-ray computed tomography imaging agent based on long-circulating bismuth sulphide nanoparticles, Nat. Mater. 5 (2006) 118–122.
[46] S. Wen, L. Zhao, Q. Zhao, L. Du, C. Liu, Z. Yu, M. Shen, J.-P. Majoral, S. Mignani, X. Shi, A promising dual mode SPECT/CT imaging platform based on ^{99m}Tc-labeled multifunctional dendrimer-entrapped gold nanoparticles, J. Mater. Chem. B 5 (2017) 3810–3815.
[47] S.Y. Yu-Sang, P.U. Atukorale, K.D. Moynihan, A. Bekdemir, K. Rakhra, L. Tang, F. Stellacci, D.J. Irvine, High-throughput quantitation of inorganic nanoparticle biodistribution at the single-cell level using mass cytometry, Nat. Comm. 8 (2017) 14069.
[48] I.C. Kourtis, S. Hirosue, A. de Titta, S. Kontos, T. Stegmann, J.A. Hubbell, M.A. Swartz, Peripherally administered nanoparticles target monocytic myeloid cells, secondary lymphoid organs and tumors in mice, PLoS One 8 (2013) e61646.
[49] M. Cataldi, C. Vigliotti, T. Mosca, M.R. Cammarota, D. Capone, Emerging role of the spleen in the pharmacokinetics of monoclonal antibodies, nanoparticles and exosomes, Int. J. Mol. Sci. 18 (2017) 1249.
[50] W.-S. Cho, M. Cho, J. Jeong, M. Choi, H.-Y. Cho, B.S. Han, S.H. Kim, H.O. Kim, Y.T. Lim, B.H. Chung, J. Jeong, Acute toxicity and pharmacokinetics of 13 nm-sized PEG-coated gold nanoparticles, Toxicol. Appl. Pharmacol. 236 (2009) 16–24.
[51] H.S. Choi, W. Liu, P. Misra, E. Tanaka, J.P. Zimmer, B. Itty Ipe, M.G. Bawendi, J.V. Frangioni, Renal clearance of quantum dots, Nat. Biotechnol. 25 (2007) 1165–1170.
[52] X.-D. Zhang, H.-Y. Wu, D. Wu, Y.-Y. Wang, J.-H. Chang, Z.-B. Zhai, A.-M. Meng, P.-X. Liu, L.-A. Zhang, F.-Y. Fan, Toxicologic effects of gold nanoparticles *in vivo* by different administration routes, Int. J. Nanomed. 5 (2010) 771–781.
[53] W.-S. Cho, S. Kim, B.S. Han, W.C. Son, J. Jeong, Comparison of gene expression profiles in mice liver following intravenous injection of 4 and 100 nm-sized PEG-coated gold nanoparticles, Toxicol. Lett. 191 (2009) 96–102.